AIAA JOURNAL
Vol. 52, No. 3, March 2014

Semi-Implicit Runge–Kutta Schemes: Development and Application to Compressible Channel Flow

Francois Kremer,* Christophe Bogey,† and Christophe Bailly‡
Ecole Centrale de Lyon, 69134 Ecully Cedex, France

DOI: 10.2514/1.J052236

Two semi-implicit six-stage Runge–Kutta algorithms are developed for the simulation of wall-bounded flows. Using these schemes, time integration is implicit in the wall-normal direction, and explicit in the other directions, to relax the time step constraint due to the fine mesh near the wall. The explicit subscheme is a six-stage fourth-order low-storage Runge–Kutta scheme. Based on analysis in Fourier space and results obtained for propagation test cases, the semi-implicit schemes are shown to be of order 3 and, for waves discretized by a number of points per period between 4 and 16, to be as accurate as, or more accurate than, the standard explicit fourth-order Runge–Kutta algorithm in terms of dissipation and dispersion. The large-eddy simulation of a compressible turbulent channel flow at a friction Reynolds number of 360 and a Mach number of 0.1 is then carried out with one of the proposed algorithms. The computational time is reduced by a factor 1.33 with respect to a large-eddy simulation using the explicit subscheme in all directions. Wall-pressure and velocity spectra from the large-eddy simulation are presented to give insights into the flow turbulent structures. In particular, wave number–frequency spectra are calculated. Acoustic components appear to be identified in these spectra.

I. Introduction

IN THE field of computational aeroacoustics (CAA), the development of direct noise computations (DNCs) has drawn attention to the need of highly accurate numerical schemes for spatial and temporal discretizations. The DNC approach indeed consists in computing both the aerodynamic and acoustic fields, by solving the compressible Euler or Navier–Stokes equations. Given that the acoustic fluctuations are by several orders of magnitude lower than the mean flow, and that they propagate over long distances, the numerical methods must be accurate and generate low dissipation and low dispersion, in order to avoid the corruption of the acoustic field. These constraints become more stringent for wall-bounded flows, which are of significant interest in CAA. The attention has in particular been drawn to wall-pressure fluctuations because they are responsible for the noise indirectly radiated inside the cabin of vehicles such as cars or aircraft, as well as the noise emitted directly in the flow over a solid boundary [1].

In the development of methods for CAA problems, the usual approach is to consider the spatial and time discretization separately. Spatial discretization methods for aeroacoustics have been proposed, among others, by Tam and Webb [2], Lele [3], and Bogey and Bailly [4]. When a discretization scheme is applied to the spatial derivatives of the Euler or Navier–Stokes equations, they reduce to the so-called semidiscretized form, which corresponds to an ordinary differential equation (ODE) of the form $d\boldsymbol{u}/dt = F(\boldsymbol{u})$, where $\boldsymbol{u}$ is the flow variable vector. Since the early papers of Runge [5] and Bashforth and Adams [6], two main families of methods have emerged to solve ODEs: the linear multistep methods and the Runge–Kutta (RK) methods. Both are used in CAA, but it can be noted that several explicit RK methods have been developed during the last decade, for instance by Bogey and Bailly [4], Hu et al. [7], Stanescu and Habashi [8], Calvo et al. [9], and Berland et al. [10]. The properties of these methods have been optimized in the Fourier space in order to minimize dissipation and dispersion errors up to frequencies close to the cutoff frequency imposed by the time step. They can be applied to many flow configurations. In wall-bounded simulations, however, the mesh is usually strongly refined close to the wall, which might lead to a severe reduction of the time step to avoid stability problems. To mention three examples, the ratios between spanwise and wall-normal mesh spacings are equal to 15 in the large-eddy simulation (LES) of a boundary layer at $Re_\theta = 300$–2000 performed by Gloerfelt and Berland [11], 18 in the LES of a channel flow at $Re_\tau = 640$ by Viazzo et al. [12], and 10 in several LESs of channel flows at $Re_\tau = 350$–960 by Kremer et al. [13]. The use of an implicit scheme, which is stable for much larger time steps, is therefore a possibility, but it implies the inversion of massive linear systems, hence a high computational cost. To reduce this cost, an iterative method is generally employed, but the choice of the method is crucial because it strongly affects the computational efficiency [14]. Furthermore, besides computational considerations, implicit time integration at large Courant–Friedrichs–Lewy (CFL) numbers can result in undesirable damping of acoustic waves [15].

An alternative is to combine an implicit scheme with an explicit scheme. The time integration of terms involving derivatives in the wall-normal direction, in which a fine mesh is implemented, is treated implicitly, whereas the time integration of the other terms is treated explicitly. Thus, the constraint on the time step is relaxed, and the additional computational cost due to the linear system inversion remains acceptable. Such methods are referred to as "semi-implicit." Because of their explicit part, the allowable CFL numbers of semi-implicit methods are much smaller than those allowed by fully implicit schemes. Thus, semi-implicit methods generally provide significantly less numerical errors compared to fully implicit schemes [16,17]. This strategy has already been used by several authors in direct numerical simulations (DNSs) of wall-bounded incompressible flows [18,19]. For example, for a turbulent boundary layer, Wu and Moin [18] used a second-order Crank–Nicholson scheme to compute convection and diffusion terms involving derivatives in the wall-normal direction, whereas the other terms were integrated in time with a third-order explicit Runge–Kutta scheme. Higher-order semi-implicit schemes have also been proposed by Simens et al. [19] and Spalart et al. [20] for incompressible problems. Because these schemes might not be relevant in the context of compressible problems, semi-implicit schemes must be developed specially for aeroacoustics. A large number of papers can be found on

Presented as Paper 2012-2066 at the 18th AIAA/CEAS Aeroacoustics Conference, Colorado Springs, CO, 4–6 June 2012; received 10 August 2012; revision received 3 July 2013; accepted for publication 9 August 2013; published online 20 October 2011.

*Ph.D. Student, Laboratoire de Mécanique des Fluides et d'Acoustique, UMR CNRS 5509; francois.kremer@ec-lyon.fr.

†CNRS Research Scientist, Laboratoire de Mécanique des Fluides et d'Acoustique, UMR CNRS 5509.

‡Professor, Laboratoire de Mécanique des Fluides et d'Acoustique, UMR CNRS 5509; Institut Universitaire de France.

so-called partitioned methods [14,21–24], which consist in applying a combination of Runge–Kutta schemes to partitioned equations. As noted in the review by Kennedy and Carpenter [24] reporting the development of semi-implicit schemes up to order 5, several ways of partitioning exist. In a first approach, partitioning is performed by gridpoint. In Kanevsky et al. [14], for instance, in order to deal with stiffness induced by grid refinement, refined portions of the mesh are solved with an implicit scheme, and coarse portions are solved with an explicit scheme. In a second approach, the equations are partitioned by term. This methodology is often used for the integration of convection-diffusion-reaction (CDR) equations [21–24]. In this case, for each point of the mesh, reactive or diffusive terms are integrated in an implicit way, and the other terms are integrated in an explicit way. Partitioning by term seems well suited for wall-bounded flow simulations as well, by treating implicitly the convection terms in the wall-normal direction, as was done in the compressible LES of Suh et al. [17]. However, these authors implemented one of the schemes developed to solve the CDR equations [23].

In the present paper, the strategy used by Kennedy and Carpenter [24] is followed in order to develop semi-implicit Runge–Kutta methods adapted to the simulation of compressible wall-bounded flows. These methods perform the time integration of terms involving wall-normal derivatives in an implicit way, whereas the other terms are integrated in an explicit way. In practice, the explicit six-stage fourth-order RK scheme of Berland et al. [10] is combined with new implicit RK schemes. The resulting algorithms are six-stage third-order semi-implicit Runge–Kutta schemes, referred to as SIRK63 in what follows. The dispersion and dissipation properties of the schemes are studied in the Fourier space, and a comparison is made with the properties of the semi-implicit scheme of Zhong [23] and of the standard explicit RK scheme of order 4. Propagation of an acoustic pulse in a two-dimensional (2-D) domain is then considered in order to quantify the degree of accuracy of these schemes. Finally, one of the SIRK63 schemes is used in the LES of a turbulent compressible channel flow at a Mach number $M = 0.1$ and a friction Reynolds number $Re_\tau = 360$ based on the half-width of the channel and the friction velocity. To illustrate the quality of the LES performed with the proposed SIRK63 algorithm on this canonical wall-bounded flow case, two important topics of wall turbulence are addressed. The first one is the scaling of near-wall turbulent structures, which have been studied by many authors, such as Tomkins and Adrian [25] for boundary layers and Jiménez et al. [26] for channel flows. The second one is closer to CAA applications because it deals with the noise induced by wall-pressure fluctuations. This problem has extensively been explored through theoretical studies using acoustic analogy [27–29] and incompressible direct numerical simulations [30,31], but only a few studies based on DNC can be found [11,17,32]. Experiments have also recently been performed by Arguillat et al. [33] among others.

The paper is organized as follows. First, the development of the semi-implicit schemes is presented in Sec. II. 2-D test cases are also shown to compare their accuracy with that of existing schemes. A three-dimensional (3-D) turbulent channel flow is simulated using one of the proposed semi-implicit schemes in Sec. III. Turbulent structures and wall-pressure fluctuations obtained are then analyzed. Finally, concluding remarks are given in Sec. IV.

II. Development of Semi-Implicit Schemes

A. Formulation

The 2-D Euler equations are considered in the present study. They can be written as

$$\frac{\partial \boldsymbol{u}}{\partial t} = -\frac{\partial \boldsymbol{E}_x}{\partial x} - \frac{\partial \boldsymbol{E}_y}{\partial y} \tag{1}$$

where $\boldsymbol{u}$ is the vector containing the flow variables and $\boldsymbol{E}_x$ and $\boldsymbol{E}_y$ are the Eulerian fluxes in the x and y directions, respectively. The equation is discretized in space, and spatial derivatives are approximated by finite differences, yielding the following semidiscretized equation:

$$\frac{\partial \boldsymbol{u}}{\partial t} = f(\boldsymbol{u}) + g(\boldsymbol{u}) \tag{2}$$

with

$$[f(\boldsymbol{u})]_{m,n} = -\frac{1}{\Delta x}\sum_{l=-N}^{M} \alpha_l [\boldsymbol{E_x}]_{m+l,n} \tag{3}$$

and

$$[g(\boldsymbol{u})]_{m,n} = -\frac{1}{\Delta y}\sum_{l=-N}^{M} \alpha_l [\boldsymbol{E_y}]_{m,n+l}$$

where (m, n) are the indices of the grid nodes, $(\alpha_l)_{l=-N,M}$ are the coefficients of the finite-difference scheme, and Δx and Δy are the uniform mesh spacings in the x and y directions, respectively. The case of a mesh strongly refined in one direction, as usually encountered in wall-bounded flows, is considered by assuming that $\Delta y << \Delta x$, so that the time integration of the term $g(\boldsymbol{u})$ raises stability concerns.

Following the strategy of Kennedy and Carpenter [24], the time integration of Eq. (2) is carried out using an s-stage semi-implicit RK scheme, which is expressed as

$$\begin{cases} \boldsymbol{u}_i & = \boldsymbol{u}_n + \Delta t \sum_{j=1}^{i-1} a_{ij}^{[E]} f(\boldsymbol{u}_j) + \Delta t \sum_{j=1}^{i} a_{ij}^{[I]} g(\boldsymbol{u}_j) \quad \text{for } 1 \le i \le s \\ \boldsymbol{u}_{n+1} & = \boldsymbol{u}_n + \Delta t \sum_{i=1}^{s} b_i^{[E]} f(\boldsymbol{u}_i) + \Delta t \sum_{i=1}^{s} b_i^{[I]} g(\boldsymbol{u}_i) \end{cases} \tag{4}$$

where $\boldsymbol{u}_n = \boldsymbol{u}(t)$, $\boldsymbol{u}_{n+1} = \boldsymbol{u}(t + \Delta t)$, Δt is the time step, $\boldsymbol{u}_i$ represents the flow variable vector at the stage i, $(a_{ij}^{[I]}, b_i^{[I]})$ are the coefficients of the implicit part of the scheme, performing the time integration of $g(\boldsymbol{u})$, and $(a_{ij}^{[E]}, b_i^{[E]})$ are the coefficients of the explicit part, for the time integration of $f(\boldsymbol{u})$. To design an s-stage SIRK method, the $s(s + 2)$ coefficients of the implicit and explicit parts must be chosen.

B. Development of the Schemes

In the present study, for the explicit part of the algorithms, the coefficients (a_{ij}, b_i) of the explicit fourth-order six-stage Runge–Kutta scheme of Berland et al. [10] are chosen, in order to take advantage of its good properties. The number of stages of the semi-implicit method is thus fixed to $s = 6$. The aim in the following is to determine the set of $s(s + 3)/2 = 27$ coefficients $(a_{ij}^{[I]}, b_i^{[I]})$ of the implicit part. Stability and accuracy constraints will be defined first. Then, the way of choosing of the coefficients will be described.

1. Order of the Implicit Part

A fourth-order accuracy is imposed to the implicit part of the scheme by applying to the coefficients $(a_{ij}^{[I]}, b_i^{[I]})$ the classical order conditions [34], which are

$$(O1) \sum_{i=1}^{s} b_i^{[I]} = 1 \qquad (O2) \sum_{i=1}^{s} b_i^{[I]} c_i^{[I]} = \frac{1}{2}$$

$$(O3)a\ \frac{1}{2}\sum_{i=1}^{s} b_i^{[I]} c_i^{[I]2} = \frac{1}{3!} \qquad (O3)b \sum_{i,j=1}^{s} b_i^{[I]} a_{ij}^{[I]} c_j^{[I]} = \frac{1}{3!}$$

$$(O4)a\ \frac{1}{6}\sum_{i=1}^{s} b_i^{[I]} c_i^{[I]3} = \frac{1}{4!} \qquad (O4)b \sum_{i,j=1}^{s} b_i^{[I]} c_i^{[I]} a_{ij}^{[I]} c_j^{[I]} = \frac{3}{4!}$$

$$(O4)c\ \frac{1}{2}\sum_{i,j=1}^{s} b_i^{[I]} a_{ij}^{[I]} c_j^{[I]2} = \frac{1}{4!} \qquad (O4)d \sum_{i,j,k=1}^{s} b_i^{[I]} a_{ij}^{[I]} a_{jk}^{[I]} c_k^{[I]} = \frac{1}{4!} \tag{5}$$

with $c_i^{[I]} = \sum_{j=1}^{i} a_{ij}^{[I]}$.

2. Coupling Conditions for Order 3

At this step, conditions (5) are now assumed to be satisfied. Ensuring that the implicit and explicit parts are both of order 4 is, however, not sufficient to obtain a fourth-order accuracy for the entire SIRK scheme. The time discretization error indeed exhibits coupling terms of lower order, which can be eliminated by imposing additional conditions. A complete description of these coupling conditions is provided by Kennedy and Carpenter [24]. For instance, order 3 can be obtained by imposing that the following coupling conditions

$$b_i^{[I]} = b_i^{[E]} = b_i \quad \text{for } 1 \le i \le s \tag{6}$$

$$\frac{1}{2}\sum_{i=1}^{s} b_i c_i^{[E]} c_i^{[I]} = \frac{1}{3!} \tag{7a}$$

$$\sum_{i,j=1}^{s} b_i a_{ij}^{[E]} c_j^{[I]} = \frac{1}{3!} \tag{7b}$$

$$\sum_{i,j=1}^{s} b_i a_{ij}^{[I]} c_j^{[E]} = \frac{1}{3!} \tag{7c}$$

with $c_i^{[E]} = \sum_{j=1}^{i-1} a_{ij}^{[E]}$, be verified. Similarly, order 4 is obtained if the coupling conditions

$$b_i^{[I]} = b_i^{[E]} = b_i \qquad \text{for } 1 \le i \le s \tag{8}$$

$$c_i^{[I]} = c_i^{[E]} = c_i \qquad \text{for } 1 \le i \le s \tag{9}$$

$$\sum_{i,j,k=1}^{s} b_i a_{ij}^{[I]} a_{jk}^{[E]} c_k = \frac{1}{4!} \tag{10a}$$

$$\sum_{i,j,k=1}^{s} b_i a_{ij}^{[E]} a_{jk}^{[I]} c_k = \frac{1}{4!} \tag{10b}$$

are imposed.

3. Stability

In the present work, the stability is examined by following the approach of Hu et al. [7] The 2-D wave equation is introduced:

$$\frac{\partial u}{\partial t} = c\left(\frac{\partial u}{\partial x} + \frac{\partial u}{\partial y}\right) \tag{11}$$

where c is the speed of sound. The spatial derivatives are evaluated using a central finite-difference scheme. A 2-D Fourier transform is then applied to Eq. (11). The effective wave numbers k_x^* and k_y^* are defined as

$$k_\xi^* \Delta\xi = 2\sum_{l=1}^{N} \alpha_l \sin\,(lk_\xi \Delta\xi) \quad \text{with} \quad \xi = x, y \tag{12}$$

and where $(\alpha_l)_{l=-N,N}$ are the coefficients of the central finite-difference scheme, Δx and Δy are the mesh spacings, and k_x and k_y are the exact wave numbers in the x and y directions. The semidiscrete equation associated with Eq. (11) can be written as

$$\frac{\partial \tilde{u}}{\partial t} = (ick_x^* + ick_y^*)\tilde{u} \tag{13}$$

where $\tilde{u}$ is the spatial Fourier transform of u, and $i = \sqrt{-1}$. When this equation is advanced in time using a SIRK scheme, with the term $ick_x^*\tilde{u}$ treated by the explicit part of the scheme, and the term $ick_y^*\tilde{u}$ treated by the implicit part, it can be shown that the amplification factor of the algorithm at each time step is given by the following linear stability function [22]:

$$R(z_x, z_y) = \frac{\tilde{u}_{n+1}}{\tilde{u}_n} = \frac{\mathrm{Det}[\boldsymbol{I} - z_x \boldsymbol{A}^{[E]} - z_y \boldsymbol{A}^{[I]} + (z_x + z_y)\boldsymbol{1} \otimes \boldsymbol{b}^T]}{\mathrm{Det}[\boldsymbol{I} - z_y \boldsymbol{A}^{[I]}]} \tag{14}$$

where $\tilde{u}_n = \tilde{u}(t)$, $\tilde{u}_{n+1} = \tilde{u}(t + \Delta t)$, $z_x = ick_x^*\Delta t$, $z_y = ick_y^*\Delta t$, $\boldsymbol{A}^{[E]} = a_{ij}^{[E]}$, $\boldsymbol{A}^{[I]} = a_{ij}^{[I]}$, $\boldsymbol{b} = b_i$, $\boldsymbol{1} = \{1, 1, \ldots, 1\}$, and $\boldsymbol{I}$ is the identity matrix. Relations (6) must be satisfied to derive this expression. The semi-implicit algorithm is stable for all combinations of z_x and z_y yielding $|R| \le 1$. Note that the amplification factors of the explicit part and of the implicit part of the algorithm are given by $R(z_x, 0)$ and $R(0, z_y)$, respectively. One important requirement is to ensure that the implicit part is unconditionally stable; hence,

$$|R(0, z_y)| \le 1 \quad \text{for } z_y \in i\mathbb{R} \tag{15}$$

The unconditional stability is difficult to obtain with an arbitrary set of the coefficients $(a_{ij}^{[I]}, b_i^{[I]})$. To overcome this problem, a singly diagonally structure is chosen for the $a_{ii}^{[I]}$ coefficients:

$$a_{ii}^{[I]} = \gamma \quad \text{for } 1 \le i \le s \tag{16}$$

where γ is a free parameter. Singly diagonally implicit RK methods [35] (SDIRK) have shown interesting features regarding stability. Kennedy and Carpenter [24] have found an interval of γ roughly equal to $0.248 \le \gamma \le 0.676$, in which condition (15) is satisfied for six-stage semi-implicit RK schemes for instance. In the present case, Eq. (9) leads to $a_{11}^{[I]} = 0$, reducing the condition (16) to $2 \le i \le s$.

4. Choice of the Coefficients $(a_{ij}^{[I]}, b_i^{[I]})$

Once the constraints ensuring accuracy and stability are defined, the 27 coefficients of the implicit part can be determined. The following approach is used. First, a value of γ ensuring condition (15) is chosen. Second, some of the coupling conditions are selected to obtain a desired order for the semi-implicit scheme. These conditions forms a nonlinear system of equations in which coefficients $(a_{ij}^{[I]}, b_i^{[I]})$ are the unknowns. This system is numerically solved by applying an iterative solver. Finally, the linear stability function (14) is evaluated so that the constructed SIRK scheme is stable for a range of (z_x, z_y) as wide as possible.

In practice, it appears that obtaining a semi-implicit scheme that exhibits both high accuracy and high stability is rather tricky. Therefore, it has been decided to determine two different sets of coefficients, focusing on either the stability or the accuracy. Thus, two semi-implicit Runge–Kutta algorithm are proposed. The one with higher stability is referred to as SIRK63-S, and the one with higher accuracy is referred to as SIRK63-A. The constraints used for the calculation of the coefficients $(a_{ij}^{[I]}, b_i^{[I]})$ are recalled in Table 1 for the two proposed schemes.

The coupling conditions (6) and (7) apply to the SIRK63-S scheme that is, therefore, of order 3. For the SIRK63-A scheme, the coupling conditions (8–10a) are imposed. Remember that conditions (8–10b) are required to ensure order 4. A set of coefficients satisfying these conditions could not be found, and consequently, the time accuracy of the SIRK63-A scheme is of order 3 only. Nevertheless, satisfying conditions (8–10a) as is the case for the SIRK63-A scheme leads to the cancellation of some terms of order 3 in the time discretization

Table 1 Constraints imposed to the coefficients of the implicit part of the SIRK63 schemes

Constraint type	SIRK63-S	SIRK63-A
SDIRK structure	$a_{ii}^{[I]} = \gamma = 0.41$	$a_{ii}^{[I]} = \gamma = 0.245$
Order 4 of the implicit part	Eq. (5)	Eq. (5)
Coupling conditions	Eqs. (6) and (7)	Eqs. (8–10a)

error, hence improving the accuracy of the SIRK63-A algorithm with respect to the SIRK63-S algorithm, which will be shown in the next section.

C. Dissipation and Dispersion Properties of the Schemes

Dissipation and dispersion of the implicit and explicit parts of the two SIRK63 algorithms are now evaluated in this section. It has been shown in the preceding section that the amplification factor of the implicit part of a SIRK algorithm is given by $R(0, ick_y^*\Delta t)$. The damping factor is derived from this expression through some variable transforms. By defining the angular frequency $\omega = ck_y^*$, the amplification factor is $G(\omega\Delta t) = R(0, i\omega\Delta t)$, and the damping factor of the implicit part is given by $1 - |G|$. Also, by introducing the effective angular frequency as $\omega^* = \arg(G)$, the dispersion error of the scheme can be measured by the quantity $|\omega^*\Delta t - \omega\Delta t|/\pi$.

Figure 1a presents the damping factor as a function of nondimensional angular frequency $\omega\Delta t$, for the implicit part of the proposed SIRK63-A and SIRK63-S algorithms, as well as for the implicit part of the ASIRK-3C scheme of Zhong [23]. The damping factor of the standard explicit fourth-order Runge–Kutta scheme (RK4) is also displayed for comparison. The SIRK63-A algorithm has a dissipation much lower than that of the other schemes. The damping factor of SIRK63-S is two orders of magnitude higher than that of SIRK63-A for the whole range of frequencies, but it is found to be similar to that of RK4. Finally, the scheme of Zhong is the most dissipative method.

Similar results are observed for the dispersion error $|\omega^*\Delta t - \omega\Delta t|/\pi$ shown in Fig. 1b. The error of the SIRK63-A scheme is almost one order of magnitude lower than that of SIRK63-S. Both are less dispersive than the RK4 and ASIRK-3C schemes, the latter showing the highest error levels again.

The damping factor and the dispersion error of the explicit part are obtained in the same preceding manner, by defining the amplification factor and the effective wave number of the explicit part as $G(\omega\Delta t) = R(i\omega\Delta t, 0)$ and $\omega^* = \arg(G)$, respectively. The damping factor and dispersion error are thus given by $1 - |G|$ and $|\omega^*\Delta t - \omega\Delta t|/\pi$, respectively. The damping factor of the different schemes is plotted as a function of the nondimensional angular frequency $\omega\Delta t$ in Fig. 2a. Note that the two SIRK63 schemes are represented by the same curve because they have the same explicit part provided by the RK46-Ber scheme [10]. Its damping factor is two orders of magnitude lower than that of RK4 and three orders of magnitude lower than that of the ASIRK-3C scheme of Zhong. The dispersion curves, given in Fig. 2b, exhibit the same tendencies. The RK46-Ber scheme is the least dispersive, with phase error one order and two orders of magnitude lower than those of RK4 and ASIRK-3C, respectively.

Finally, the present study shows that, for nondimensional angular frequencies in the range $\pi/8 \le \omega\Delta t \le \pi/2$, the accuracy of the semi-implicit schemes proposed in this paper is higher than that of the semi-implicit scheme of Zhong [23] and at least as good as that of the standard RK4 scheme. For $\omega\Delta t < \pi/8$, that is, for waves discretized by more than 16 points per period, the SIRK63-S scheme is less accurate than the RK4 scheme because of its lower order. However, in this case, the error levels obtained for both schemes are inferior to 10^{-5}. The apparent low accuracy of the ASIRK-3C scheme is due to the fact that this method was initially developed for the simulation of transient hypersonic flows with thermochemical nonequilibrium, in which viscous stress, heat flux or reaction source terms are treated by the implicit subscheme. The scheme of Zhong is thus a priori not adapted to the time integration of convective terms without dissipation and without dispersion. However, to the authors' knowledge, the only case of aeroacoustics problem solved in a semi-implicit way used the ASIRK-3C scheme [17]. For this reason, the SIRK63 algorithms developed here are compared to the scheme of Zhong.

D. Test Cases

1. Definition

The properties of the semi-implicit schemes are first investigated by considering the propagation of an acoustic pulse in a medium at rest. In this test case, the 2-D Euler equations are solved on different anisotropic Cartesian meshes. The mesh spacings in the x and y directions are Δx and Δy, respectively. In what follows, Δx is fixed, whereas $\Delta y \le \Delta x$ is different for each mesh. The number of grid

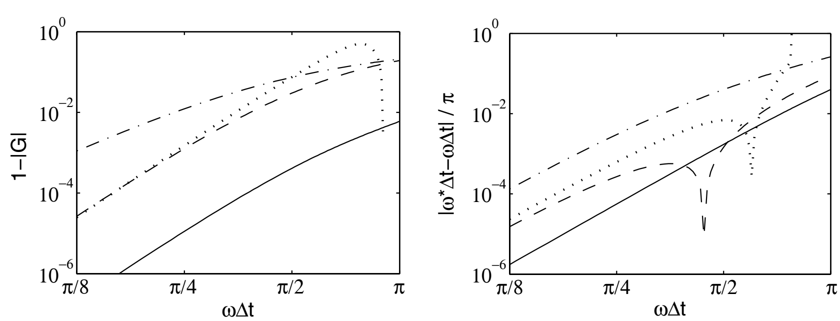

a) b)

Fig. 1 a) Damping factor and b) dispersion error per time step of the implicit part of the schemes, as a function of nondimensional frequency $\omega\Delta t$. –. –.: ASIRK-3C of Zhong [23], ...: standard RK4, proposed schemes: ———: SIRK63-A and – – –: SIRK63-S.

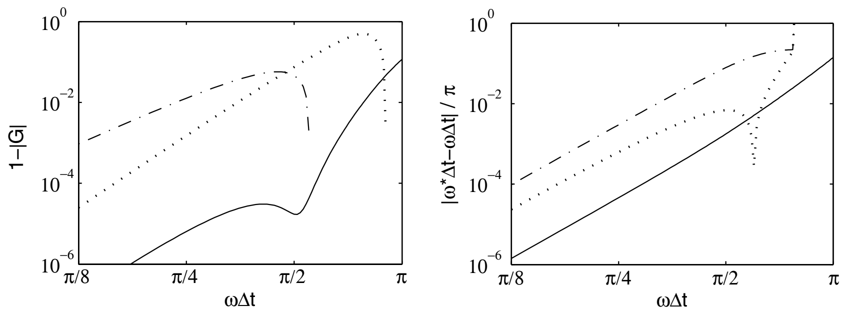

a) b)

Fig. 2 a) Damping factor, and b) dispersion error per time step of the explicit part of the schemes, as a function of nondimensional frequency $\omega\Delta t$. –. –.: ASIRK-3C of Zhong [23], ...: standard RK4, ———: proposed SIRK63-A and SIRK63-S (RK46-Ber of Berland et al. [10]).

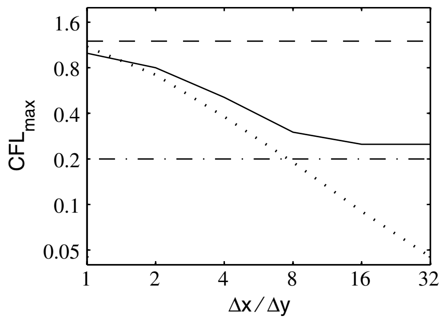

Fig. 3 Maximum CFL number of the time integration schemes, as a function of the aspect ratio $\Delta x/\Delta y$. –. –.: ASIRK-3C of Zhong [23], ...: standard RK4, proposed schemes: ——: SIRK63-A and – – –: SIRK63-S.

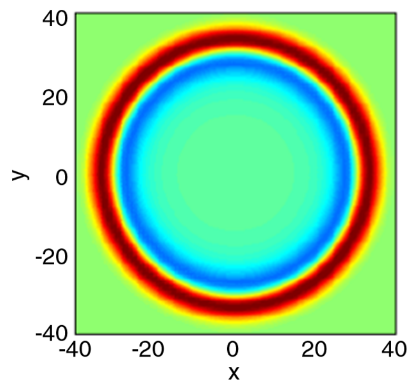

Fig. 4 Fluctuating pressure field, at $t = 32\Delta x/c$, of the reference simulation for the acoustic pulse case, run with the RK4 time integration scheme, for $\Delta x/\Delta y = 1$ and CFL $= 0.01$. The color scale ranges between ± 1 Pa.

points in each mesh is $140 \times 140 \times \Delta x/\Delta y$. The initial conditions are defined by

$$
\begin{aligned}
p &= p_0 + \Delta p \exp[-\ln(2)(x^2 + y^2)/b^2] \\
\rho &= \rho_0 + (p - p_0)/c^2 \\
u_x &= u_y = 0
\end{aligned}
\tag{17}
$$

where $b = 3\Delta x$, $p_0 = 10^5$ Pa, $\Delta p = 10$ Pa, $c = \sqrt{\gamma p_0/\rho_0}$, $\rho_0 = p_0/(T_0(\gamma - 1)c_v)$, $T_0 = 293$ K, and $c_v = 717.5$ J $\cdot$ K^{-1} $\cdot$ kg^{-1}. To obtain spatial discretization errors negligible with respect to time integration errors, a 21-point centered finite-difference scheme of order 20 is used.

The stability limit of the time integration algorithms is evaluated on a set of simulations with periodic boundary conditions, such that the centered finite-difference scheme is used in the entire mesh. A second set of simulations are then carried out to study the accuracy of the algorithms, using nonreflective boundary conditions [36] combined with low dissipative and low dispersive noncentered finite differences [37] at the boundaries of the domain.

Simulations are performed with the time integration schemes SIRK63-S, SIRK63-A, ASIRK-3C, and RK4 for aspect ratios $\Delta x/\Delta y = 2$, 4, 8, 16, and 32. The terms containing y derivatives in the Euler equations are integrated by the implicit part of the algorithm, whereas the other terms are integrated with the explicit part when semi-implicit schemes are used. The CFL number is defined as CFL $= c\Delta t/\Delta x$.

2. Stability

The aim here is to numerically find the maximum CFL number ensuring stability. These values of CFL_{max} are plotted in Fig. 3 as a function of the aspect ratio, for the different schemes. The axes are in logarithmic scale. The proposed SIRK63 schemes appear to be the most stable. The SIRK63-S scheme exhibits the highest value of $CFL_{max} = 1.2$ at all aspect ratios. Concerning SIRK63-A, the maximum CFL number is found to decrease with Δy, before reaching a plateau at $CFL_{max} = 0.25$, a value slightly higher than that of the scheme of Zhong [23], for which $CFL_{max} = 0.2$ at all aspect ratios. For the explicit RK4 scheme, the maximum CFL number decreases as Δy decreases, as expected.

3. Accuracy

Simulations are now carried out up to $t = 32\Delta x/c$, for CFL numbers varying from 0.1 to 1. Their results are compared with reference simulations. Because the grids change with the aspect ratio, one reference simulation is run for each grid with a very small CFL number. The CFL number is, for instance, equal to 10^{-1} for $\Delta x/\Delta y = 1$ and to 10^{-4} for $\Delta x/\Delta y = 32$. As an illustration, the reference solution computed on the grid with $\Delta x/\Delta y = 1$ is shown in Fig. 4.

The accuracy of the schemes is estimated by the error rate E, defined as follows:

$$
E = \frac{\sqrt{\iint_S (p - p_{\mathrm{ref}})^2 \,\mathrm{d}s}}{\sqrt{\iint_S (p_{\mathrm{ref}} - p_0)^2 \,\mathrm{d}s}} \tag{18}
$$

where p_{ref} is the reference solution. Error rates obtained using different schemes for values of $\Delta x/\Delta y$ equal to 1 and 32 are plotted in Figs. 5a and 5b, respectively. The axes are in logarithmic scale. The results being very similar, the analysis is limited to the case $\Delta x/\Delta y = 1$, displayed in Fig. 5a. The SIRK63-A scheme has the best accuracy, with an error rate one order of magnitude lower than that of SIRK63-S and of RK4. The ASIRK-3C scheme has the weakest accuracy, its error rate being more than one order of magnitude higher than that of SIRK63-S. These results are in good agreement with the theoretical study in Sec. II.C. Finally, a reference slope of order 3 is provided as a gray line to evaluate the order of the error rates. Those of the semi-implicit schemes are of order 3 for low

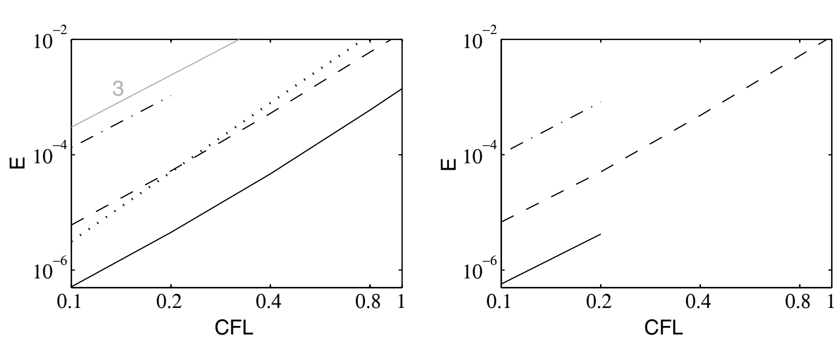

Fig. 5 Error rate E of the time integration schemes, at $t = 32\Delta x/c$, for the acoustic pulse case: a) $\Delta x/\Delta y = 1$ and b) $\Delta x/\Delta y = 32$. .–.–.: ASIRK-3C of Zhong, ...: standard RK4, proposed schemes: ——— SIRK63-A and – – –: SIRK63-S.

CFL numbers. The SIRK63 algorithms present a steeper slope for CFL > 0.4.

To highlight the coupling effects between the explicit and implicit parts of the SIRK algorithms, snapshots of the error $(p - p_{\mathrm{ref}})/E$, are shown in Fig. 6, for simulations performed with CFL $= 0.1$ and $\Delta x/\Delta y = 1$. As expected, the error is isotropic for the RK4 scheme in Fig. 6a because the same algorithm is used in the x and y directions. Inversely, the semi-implicit schemes exhibits anisotropy. The error of the ASIRK-3C scheme plotted in Fig. 6b is dominant in the directions parallel to the axes of the mesh, whereas the proposed SIRK63-A and SIRK63-S schemes in Figs. 6c and 6d provide the largest errors in the diagonal directions.

It must be noted that different results can be obtained at other values of the CFL number and of $\Delta x/\Delta y$. Figure 7a shows, for instance, the error of the SIRK63-S scheme for $\Delta x/\Delta y = 1$ and CFL $= 1$. Compared to the error at CFL $= 0.1$ in Fig. 6c, the pattern clearly changes. The influence of the aspect ratio is also highlighted by the comparison of Figs. 7a and 7b, corresponding to $\Delta x/\Delta y = 1$ and 32, for CFL $= 1$. It can be seen that the aspect ratio has a very small effect on the anisotropy of the error.

E. Summary

Some properties of the schemes developed in this paper are summarized in Table 2, which reports the maximum CFL number and the error rate E at CFL $= 0.2$ for aspect ratios of 1 and 32. The proposed SIRK63-S algorithm appears to be the most stable, with a maximum CFL number of 1.2 independent of the aspect ratio. The SIRK63-A is less stable, with a maximum CFL number decreasing from 1 to 0.25 when the aspect ratio increases. However, it remains more stable than the scheme ASIRK-3C of Zhong [23], which has a maximum CFL number of 0.2. Concerning accuracy, the SIRK63-A scheme is more accurate than SIRK63-S: the former has error rates more than one order of magnitude lower than the latter. The accuracy of SIRK63-S is similar to that of RK4 and is better than that of the scheme of Zhong.

The SIRK63 schemes consume six stages per time step, which is two times more than a standard three-stage RK scheme and 1.5 times more than a standard four-stage RK scheme. However, to compare the computational efficiency of these schemes, it appears necessary to consider the ratio between the maximum CFL number and the number of stages s. This quantity is given in Table 3. For the

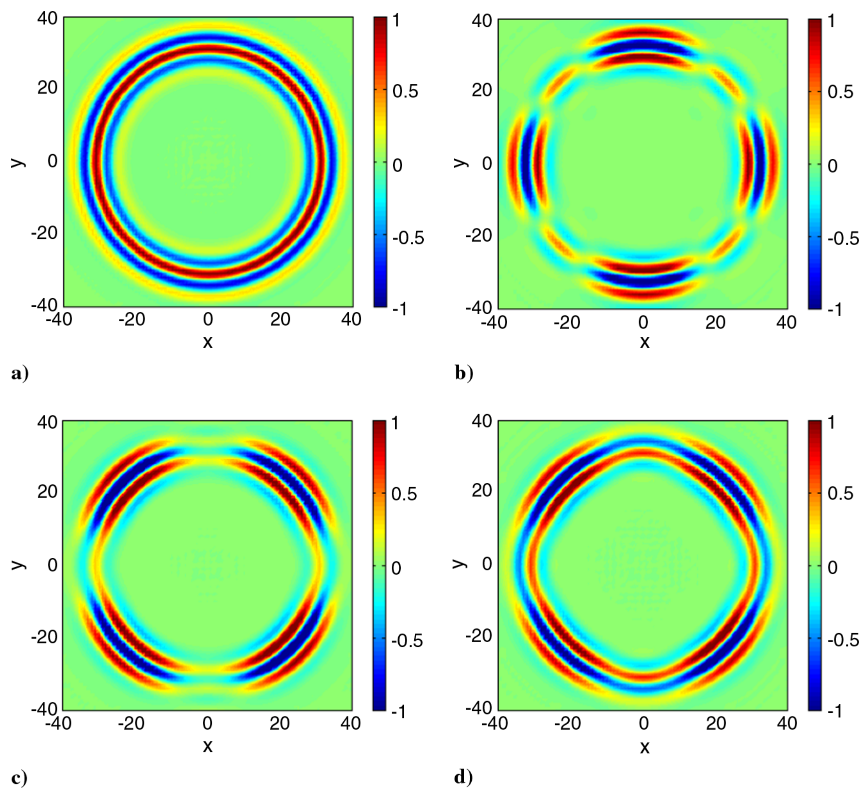

Fig. 6 Snapshots of $(p - p_{\mathrm{ref}})/E$ to illustrate the anisotropy of the error, where p_{ref} is the reference solution and p is the pressure computed at CFL $= 0.1$ and $\Delta x/\Delta y = 1$ using a) standard RK4, b) ASIRK-3C of Zhong [23], and proposed schemes c) SIRK63-S and d) SIRK63-A.

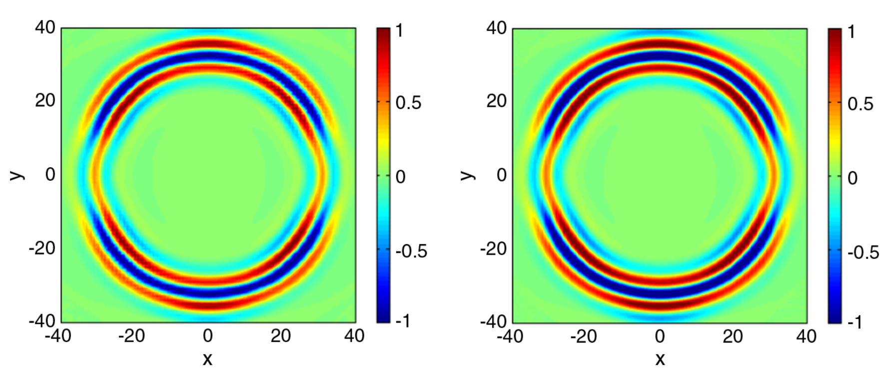

Fig. 7 Snapshots of $(p - p_{\mathrm{ref}})/E$ to illustrate the anisotropy of the error, where p_{ref} is the reference solution and p is the pressure computed using SIRK63-S at CFL $= 1$ on meshes with aspect ratio of a) $\Delta x/\Delta y = 1$ and b) $\Delta x/\Delta y = 32$.

Table 2 Maximum CFL numbers and error rate obtained for the different schemes, as a function of the aspect ratio $AR = \Delta x / \Delta y$

	CFL_{max}		E (CFL = 0.2)	
Scheme	AR = 1	AR = 32	AR = 1	AR = 32
SIRK63-S	1.2	1.2	4.9×10^{-5}	5.0×10^{-5}
SIRK63-A	1.0	0.25	4.1×10^{-6}	4.2×10^{-6}
ASIRK-3C	0.2	0.2	8.2×10^{-4}	8.2×10^{-4}
RK4	1.1	0.045	4.4×10^{-5}	— —

Table 3 Number of stages s and ratio between the maximum CFL number and the number of stages obtained for the different schemes, as a function of the aspect ratio $AR = \Delta x / \Delta y$

		CFL_{max}/s	
Scheme	s	AR = 1	AR = 32
SIRK63-S	6	0.2	0.2
SIRK63-A	6	0.17	0.042
ASIRK-3C	3	0.067	0.067
RK4	4	0.28	0.011

SIRK63-S scheme, the ratio CFL_{max}/s is equal to 0.2 for all aspect ratios, whereas for the RK4 scheme it decreases from 0.275 to 0.011 when the aspect ratio increases from 1 to 32. The SIRK63-S scheme is thus slightly less efficient than the RK4 scheme for low aspect ratios, but it is much more efficient for high aspect ratios.

III. Simulation of a Plane Channel Flow

A. Parameters

A channel flow at a friction Reynolds number $Re_\tau = hu_\tau/\nu = h^+ = 360$ and a centerline Mach number $M_0 = U_0/c = 0.1$ is computed by LES, where h is the half-width of the channel, $u_\tau = \sqrt{\tau_w/\rho}$ is the friction velocity based on the wall shear stress τ_w and the density ρ, ν is the kinematic molecular viscosity, U_0 is the centerline velocity, and c is the speed of sound. The dimensions of the channel are $L_x \times L_y \times L_z = 12h \times 2h \times 6h$.

At time $t = 0$, laminar Blasius profiles with thickness $\delta_0 = 0.4h$ are imposed for the streamwise velocity. Spanwise and wall-normal velocities are set to zero. Static pressure and temperature are uniform in the entire domain, with $p_0 = 10^5$ Pa and $T_0 = 293$ K. The flow is driven by a mean pressure gradient, which is given by a body force in the streamwise direction $\rho \times f = \tau_w / h$. The transition toward a turbulent flow is triggered by adding velocity fluctuations in the Blasius velocity profiles, following a method initially developed by Bogey et al. for pipe flows [38].

B. Numerical Methods

The LES is performed by solving the compressible Navier–Stokes equations, using low-dissipation and low-dispersion 11-point finite differences for spatial derivatives [4,37]. Periodic boundary conditions are implemented in the x (streamwise) and z (spanwise) directions. In the y (wall-normal) direction, a no-slip boundary condition is imposed at the wall. The dissipative effects of the subgrid motions are taken into account by the use of an explicit 11-point filter of order 6 [39], removing the smallest discretized scales, while leaving the well-resolved scales nearly unaffected. More details about this approach can be found in [40,41]. The simulation is carried out on a Cartesian grid, with constant mesh spacings in the streamwise and spanwise directions, equal to $\Delta x^+ = 16.6$ and $\Delta z^+ = 8.3$ in wall units. In the wall-normal direction, the mesh spacing is stretched using an expansion rate $r = 1.0442$, yielding values of Δy^+ from 0.95 at the walls up to 15.8 at the center of the channel. The number of grid points is $n_x \times n_y \times n_z = 257 \times 133 \times 257 = 8.8$ million points.

The time integration is performed by the semi-implicit scheme SIRK63-S developed in Sec. II. The implicit part of the scheme is used for the convective terms involving y derivatives, whereas the explicit part of the scheme applies to the other terms. The time step $\Delta t \approx 2.05 \times 10^{-7}$ s is chosen such as $CFL_z = c\Delta t/\Delta z = 1$ to ensure stability of the explicit part of the SIRK63-S algorithm. Then, the maximum CFL number, at which the implicit part of the scheme is used, is $CFL_y = c\Delta t/\Delta y = 8.7$ at the wall. To reduce the CPU time, the semi-implicit scheme is applied to regions of the grid where $\Delta y < \Delta z$, that is, for grid points close to the wall. Outside these regions, the value of CFL_y is smaller than 1 so that no implicit time integration is needed. All the convective terms, including those containing y derivatives, are here integrated with the explicit RK46-Ber scheme.

The simulation is carried out on a shared-memory computer SGI ALTIX UV 1000. The CPU time of the algorithm is compared with that of the same case computed using an explicit RK scheme. For that simulation, the RK46-Ber scheme is used, with a CFL number $CFL_y = 1$ at the walls, yielding a time step $\Delta t \approx 2.37 \times 10^{-8}$ s. When the computation runs on a single CPU core, the fully explicit simulation is about 1.6 times faster than the semi-implicit one, which is severely penalized by the inversion of the linear systems. However, the semi-implicit algorithm becomes more efficient when the code is parallelized with the OpenMP library on several cores. This can be seen in Fig. 8a, which presents the speedup of the parallelized algorithms as a function of the number of cores. The speedup of the semi-implicit algorithm is close to the ideal case up to 12 cores, whereas the speedup of the fully explicit algorithm is smaller. CPU times using the semi-implicit and fully explicit algorithms are shown in Fig. 8b for a simulation over a physical time of 10^{-6} s, using logarithmic scale for the axes. For a number of cores smaller than 6, the semi-implicit algorithm is slower than the explicit algorithm, which is due to the high cost in CPU time induced by the inversion of the linear systems. When the number of cores increases, the difference between the CPU time of the two algorithms becomes smaller. For more than 6 cores, the semi-implicit algorithm is then faster than the explicit one. Using 12 cores, the computational time of the SIRK algorithm is about 1.33 times smaller than that of the fully explicit algorithm. These results have been obtained for a parallelization in the z direction, in which the number of points $n_z = 257$ results in a number of points per core in the z direction

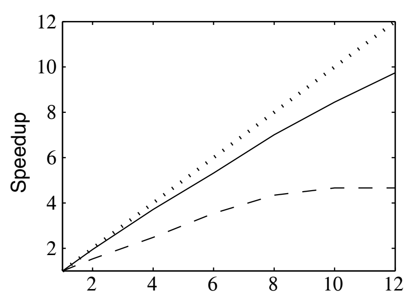

a)

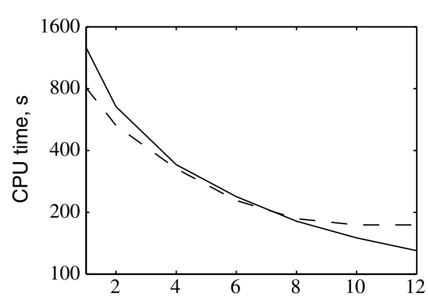

b)

Fig. 8 a) Speedup and b) CPU time for a simulation over a physical time of 10^{-6} s s. – – –: RK46-Ber, ———: SIRK63-S.

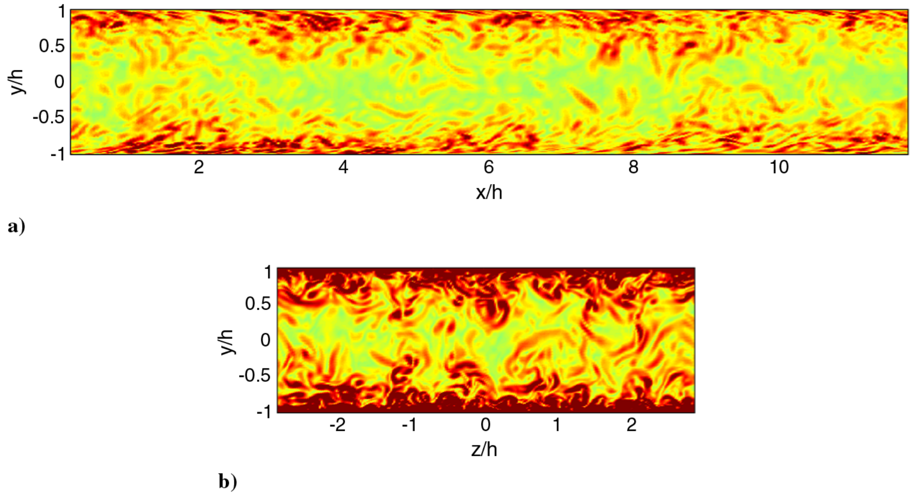

Fig. 9 Snapshot of the vorticity norm in the a) x-y plane and b) z-y plane. The color scale ranges up to $3 \times 10^4\ \mathrm{s}^{-1}$.

smaller than 32 for more than 8 CPUs. Thus, the communication between processors is significant, leading to a negligible speedup as observed for the explicit algorithm, and as would be observed for the semi-implicit algorithm for a higher number of cores.

C. Flowfield

Snapshots of the vorticity field in x-y and z-y planes are shown on Figs. 9a and 9b, respectively. Turbulence is seen to be fully developed through the height of the channel. The near-wall regions exhibit structures of small size and intense vorticity, whereas the structures at the midheight of the channel are less intense and greater in size.

Figures 10a and 10b present the profiles of mean streamwise velocity and of streamwise fluctuation intensity, respectively, as a function of the distance to the wall. Wall scaling is used for the mean velocity $U^+ = U/u_\tau$, fluctuation intensity $u'^+ = \sqrt{\overline{u'u'}}/u_\tau$, and wall distance $y^+ = yu_\tau/\nu$. The wall distance is represented in logarithmic scale. Data from the channel flow simulation at $Re_\tau = 395$ of Moser et al. [42] are also reported. A very good agreement with the DNS date is found for both mean and fluctuating velocities. The peak rms velocity is in particular well predicted at $y^+ = 13.2$.

D. Definition of Spectra

For spectral analysis, data from the LES are stored over a time period of $70h/U_0$. Including the time of the transition to a fully turbulent state, the total duration of the simulation is equal to $140h/U_0$. Every fifth time step, samples of pressure at the walls and of velocity components in wall-parallel planes are collected. The location of these planes are $y^+ = 18$ and 105 in wall units and $y/h = 0.05$ and 0.3 in outer units. The first plane is close to the location of the maximum rms velocity. The database thus contains time–space samples, noted $q(x_i, z_j, t_n)$; $1 \le i \le n_x$; $1 \le j \le n_z$; $1 \le n \le N$, where $N = 6000$ is the number of time samples. The quantity q represents either the wall pressure or a velocity component in one of the planes in which data are collected. For each of these variables, a 3-D spectrum $\hat{q}(k_x, k_z, \omega)$ is obtained, as a function of streamwise and spanwise wave numbers k_x and k_z and of angular frequency ω. To render the spectrum smoother, the database is subdivided into five overlapping time segments of length $N_S = 2000 \times$ $(T_S = 24h/U_0)$. Spectra are then computed on each segment and averaged to provide the final 3-D spectrum. Power spectral densities are finally obtained as $\Phi_{qq} = \hat{q}\hat{q}^*/(L_x L_z T_S)$. The frequency range is $0.014 \le \omega^+ = \omega\nu/u_\tau^2 \le 14.4$, and the wave number ranges are $0.0015 \le k_x^+ = k_x\nu/u_\tau \le 0.18$ and $0.0031 \le k_z^+ = k_z\nu/u_\tau \le 0.38$.

E. Turbulent Structures

The power spectral densities of the three components of velocity in the plane located at $y^+ = 18$ are shown in Fig. 11a as a function of the spanwise wave number in wall units k_z^+. The axes are in logarithmic scale. The spectra levels present great disparity between the components, indicating the strong anisotropy of the velocity fluctuations in the near-wall region. The streamwise component dominates for all wave numbers, its level being one order of magnitude higher than that of the spanwise component. The wall-normal component is the less energetic, its level being two order of magnitude lower than that of the spanwise component, except in the high wave-number region in which both have the same levels. The sharp collapse of the spectra observed for $k_z^+ > 0.15$ is due to the spectral truncation of the filtered LES. A quantitative estimation of the scales damped by the relaxation filter will be presented later.

The spectrum of the streamwise velocity has a maximum around $k_z^+ \approx 0.02$, whereas the spectrum of the wall-normal velocity component has a peak at $k_z^+ = 0.05$. These results are typical marks

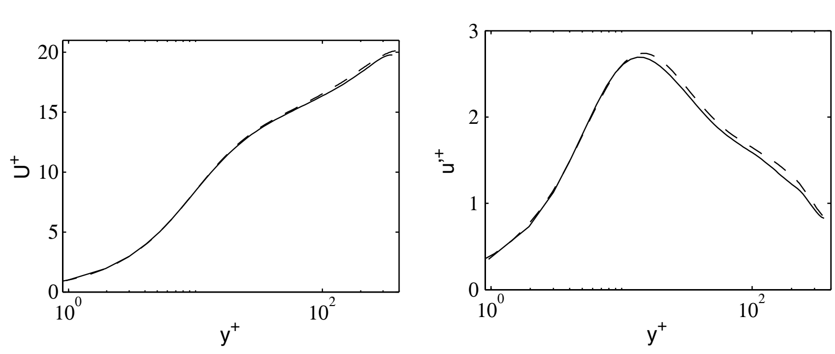

Fig. 10 a) Mean streamwise velocity $U^+ = U/u_\tau$ and b) streamwise fluctuation intensity $u'^+ = \sqrt{\overline{u'u'}}/u_\tau$ as functions of the wall distance $y^+ = yu_\tau/\nu$. – – –: DNS of Moser et al. [42] at $Re_\tau = 395$, ———: present LES.

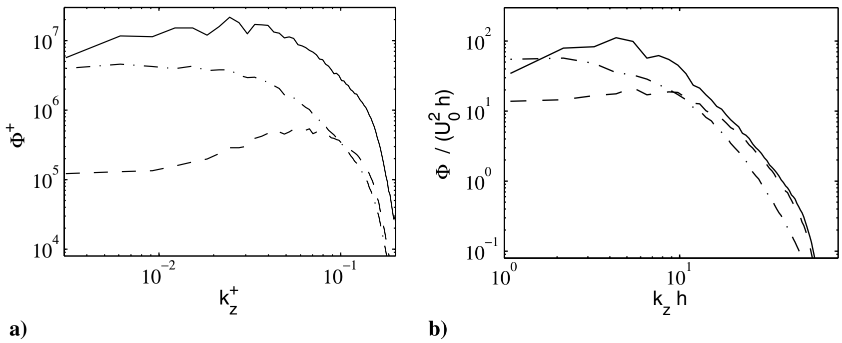

Fig. 11 Power spectral densities of the velocity fluctuations as functions of k_z at a) $y^+ = yu_\tau/\nu = 18\ (y/h = 0.05)$ and b) $y^+ = 105\ (y/h = 0.3)$. ———: Φ_{uu}, – – –: Φ_{vv}, –.–.: Φ_{ww}.

of the near-wall streaks, which consist of alternating regions of high and low streamwise velocity elongated in the streamwise direction [43]. The maximum spanwise wave number $k_z^+ \approx 0.02$ provides an average spacing of the most energetic streaks of $\lambda_z^+ \approx 300$. These structures are accompanied by quasi-streamwise vortices, which induce the peak visible in the spectrum of the wall-normal velocity at $k_z^+ = 0.05$.

It can be noticed here that the spanwise spacing of the near-wall streaks is higher than the value of 100 wall units usually observed in the literature [44]. This figure, which was verified by many other studies [43], is, however, obtained from flow visualizations, which do not necessarily provide the size of the most energetic structures. A similar shift has been indeed noted by Tomkins and Adrian [25] in boundary layers at $Re_\tau = 426$, in which the most energetic scales were found to range over $200 \le \lambda_z^+ \le 400$ at $y^+ = 21$.

The spectra obtained further from the wall, at $y^+ = 105$, or $y = 0.3h$ in outer units, are shown in Fig. 11b, as a function of the spanwise wave number. Outer scaling is applied to the axes, using the half-width of the channel h, and the centerline velocity U_0. The velocity field is observed to be more isotropic than in Fig. 11a. However, anisotropy persists at low wave numbers because the wall-normal component of the velocity is significantly less energetic than the other components for $k_z h < 7$. Regarding the streamwise component, the spectrum appears to be dominated by lower wave numbers compared to the near-wall spectrum. Indeed, the peak is located at $k_z h = 5.4$, corresponding to a wavelength $\lambda_z = 1.2h$, or $\lambda_z^+ \approx 420$ in wall units. This value is higher than that provided by Tomkins and Adrian from boundary-layer experiments, who measured the most energetic scales around $\lambda_z \approx 0.8\delta$, at $y = 0.2\delta$, with δ the boundary-layer thickness [25]. However, the authors pointed out that the largest scales in boundary layers and in channel flows should exhibit differences because of the influence of the geometry of the facility. Comparison can also be made with the LES results of Bogey et al. for a tripped nozzle pipe flow [38]. Just downstream of the exit, the azimuthal modes of the streamwise velocity are noticed to be the most energetic at $k_\theta \delta \approx 7$ [45].

F. Wall-Pressure Spectra

The wall-pressure frequency spectrum $\Phi_{pp}(\omega)$, shown in Fig. 12, is obtained by integration of the 3-D spectrum over k_x and k_z. The axes are in logarithmic scales, and the coordinates are given in wall units. The spectrum has been premultiplied by the angular frequency ω to highlight the separation between high- and low-frequency regions. For low frequencies, the premultiplied spectrum increases with ω, following a power law with an exponent equal to 6/5, as illustrated by the dashed line. The spectrum reaches a peak at a nondimensional angular frequency $\omega^+ = 0.3$ and then rapidly decreases for higher frequencies. A slope of order ω^{-4} indicated in the figure by a dash-dot line can be noticed in a small range of frequencies $\omega^+ \approx 0.8$–1, which is consistent with the decay in ω^{-5} observed for Φ_{pp} in a number of boundary-layer experiments [46]. The decay becomes sharper for $\omega^+ \ge 1$, which can be attributed to the dissipative effect of the relaxation filter of the LES, for which the cutoff wave number is $k_x \approx 2\pi/(4\Delta x)$ in the streamwise direction.

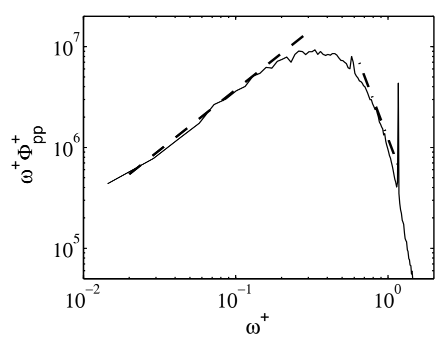

Fig. 12 Power spectral density of the wall-pressure fluctuations as a function of $\omega^+ = \omega\nu/u_\tau^2$. – – –: $\omega^{6/5}$, –.–.: ω^{-4}.

Assuming a Taylor hypothesis of frozen turbulence convected at a speed roughly equal to $u_c = 0.7U_0$, the nondimensional cutoff angular frequency is equal to $\omega\nu/u_\tau^2 \approx 1.3$, which corresponds well to the frequency at which a strong decrease is observed in the figure. Integration of spectrum over ω finally provides the rms pressure, for which the nondimensional value is equal to $p_{\mathrm{rms}}/\tau_w = 2.3$. All these results are in good agreement with the study conducted by Hu et al. [47] on DNS data. Two unexpected peaks with narrow bandwidth appear at frequencies $\omega^+ = 0.58$ and 1.17. These peaks are related to acoustic components. Their origin will be discussed in view of a 2-D spectrum.

A 2-D spectrum of the pressure fluctuations obtained by integration of the 3-D spectrum over k_z is plotted in Fig. 13a, as a function of the streamwise wave number k_x and angular frequency ω, scaled by the centerline velocity U_0 and the channel half-width h. Similarly, integration of the 3-D spectrum over k_x provides the 2-D spectrum given in Fig. 13b, as a function of the spanwise wave number k_z and ω. A well-known feature in wave number–frequency power spectra of wall-pressure fluctuations is the convective ridge, corresponding to the footprint of the turbulent structures convected by the mean flow. This ridge consists of a strong peak, which has been observed by early measurements such as those of Willmarth and Wooldridge [48]. The construction of most wall-pressure models is based on this result [1], which has also been reproduced by incompressible numerical simulations [12,49,50]. In Fig. 13a, the convection ridge is clearly visible around wave numbers $k_x = \omega/u_c$, which are indicated by a dash-dot line. The slope of the convection ridge provides the convection speed $u_c = 0.7U_0$, used in the preceding paragraph for the frozen turbulence hypothesis. The ridge is not visible on the k_z-ω spectrum presented in Fig. 13b, as expected, because there is no convection effect in the spanwise direction. Hence, the k_z-ω spectrum is symmetric with respect to $k_z = 0$.

The low–wave number region of the 2-D spectra is also of interest, as noted by Bull [1], because it contributes to the structural excitation and radiated noise. The latter is generated by components contained in the supersonic region of the wave number–frequency spectrum, delimited by $k_x^2 + k_z^2 \le (\omega/c - k_x M_c)^2$ with $M_c = u_c/c$. Because the present 2-D spectra are obtained by integration over k_z or k_x, the

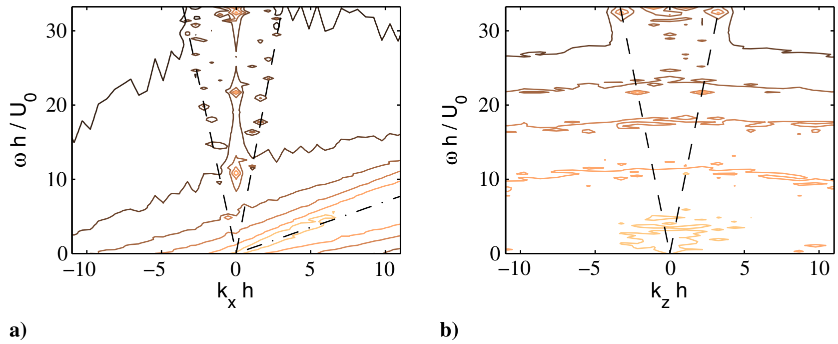

Fig. 13 Power spectral density of the wall-pressure fluctuations as a function of $\omega h/U_0$ and a) $k_x h$ and b) $k_z h$. Two consecutive isolines represent a magnitude ratio of 6.4. –.–.: convective wave number $k_x = \omega/u_c$ with $u_c = 0.7U_0$, – – –: convected acoustic wave numbers a) $k_x = \omega/(u_c \pm c)$ and b) $k_z = \pm\omega/c$.

limits of the supersonic region reduce to $k_x = \omega/(c \pm u_c)$ for the k_x-ω spectrum and to $k_z = \pm\omega/c$ for the k_z-ω spectrum. These sonic lines are denoted by the dashed lines in Figs. 13a and 13b.

The peaks found inside the supersonic region represent the footprint of the acoustic waves computed directly by the compressible LES. The two peaks previously observed on the one-dimensional frequency spectrum in Fig. 12 are found in the k_x-ω spectrum in Fig. 13a at $k_x = 0$ and $\omega h/U_0 = 10.7$ and 21.4. A third harmonic can be noticed at $\omega h/U_0 = 33$. These components do not propagate in the streamwise direction because they have an infinite phase speed ω/k_x. In the k_z-ω spectrum in Fig. 13b, two peaks are noted at the frequency of the second harmonic $\omega h/U_0 = 21.4$, on the sonic lines. Two peaks are also found at the third harmonic $\omega h/U_0 = 33$. This implies that these components are due to acoustic waves traveling in the spanwise direction. The presence of peaks at the frequency of the first harmonic $\omega h/U_0 = 10.7$ is less visible. A greater number of other peaks are found in the supersonic region of the k_x-ω spectrum in Fig. 13a, for $k_x \neq 0$ and $\omega h/U_0 > 10$. For lower frequencies, acoustic contributions cannot be distinguished, and the spectrum is dominated by the convective ridge.

IV. Conclusions

In this paper, two semi-implicit schemes of order 3, referred to as SIRK63-A and SIRK63-S, are designed for the computation of wall-bounded compressible turbulent flows. Their explicit subscheme is based on the explicit algorithm of Berland et al. [10] Their respective implicit subschemes are unconditionally stable and allow to perform the time integration of the flux-governing equations in the direction in which the mesh is refined without decreasing the time step significantly. The damping factor and dispersion error of the SIRK63-A and SIRK63-S algorithms are shown to be smaller or similar to those of the standard Runge–Kutta scheme of order 4 for wave components discretized by a number of points per period between 4 and 16. Numerical tests illustrate the stability property of these schemes. In particular, the stability limit of SIRK63-S is independent of the mesh refinement. The SIRK63-S algorithm is then used in an LES of a compressible turbulent channel flow at $Re_\tau = 360$ and $M = 0.1$. The profiles of the mean and fluctuating velocities are in good agreement with DNS data from the literature. Velocity spectra are computed from the LES data, at two different distances to the wall. The spanwise spacing of the turbulent structures appears to be slightly larger in this channel flow case compared to the results observed in turbulent boundary layers [25]. Wall-pressure fluctuations are also examined. The streamwise wave number–frequency spectrum displays the expected convective ridge, and some acoustic components are also detected in the low-wave number region. This point illustrates the ability of the compressible LES to compute directly the noise generated by a turbulent wall-bounded flow.

Acknowledgments

The first author is grateful to the Direction Générale de l'Armement and the Centre National de la Recherche Scientifique for financial support. This work was granted access to the HPC resources of the Institut du Développement et des Ressources en Informatique Scientifique under the allocation 2011-020204 made by Grand Equipement National de Calcul Intensif. The authors would like to thank Olivier Marsden for his help on the parallelization of the code with the OpenMP library.

Appendix: Six-Stage Fourth-Order Semi-Implicit Runge–Kutta Schemes

In this appendix, the coefficients of the implicit part of the semi-implicit algorithms are listed in Fig. A1 for the SIRK63S scheme and

$a_{ij}^{[I]}$	0.41					
	-0.050847598260407	0.41				
	-0.732843054288974	0.488808741097800	0.41			
	0.518289378427379	-1.277080692402156	0.558980743308365	0.41		
	-0.802531364350514	0.646260865229491	0.497772202911395	-0.379275265944952	0.41	
	-0.518537243124588	0.051438098423723	0.611601988166285	0.227118479918187	0.120091948181429	0.41
$b_i^{[I]}$	0.971001746640224	-1.272664996516041	1.282112737365169	-1.209258255434315	0.958808767944964	0.27

Fig. A1 Coefficients of the implicit part of the SIRK63-S scheme.

$a_{ij}^{[I]}$	0					
	-0.212081394856242	0.245				
	-0.506934417330455	0.511286140669274	0.245			
	-3.2	3.622080130757558	-0.200168425700507	0.245		
	0.273655978647576	-0.810460387252415	1.516528920894552	-0.642694098243515	0.245	
	0.272572117804249	0.001343810878341	-0.020976057113187	-0.117426001935445	0.466739114149427	0.245
$b_i^{[I]}$	0.971001746640224	-1.272664996516041	1.282112737365169	-1.209258255434315	0.958808767944964	0.27

Fig. A2 Coefficients of the implicit part of the SIRK63-A scheme.

	0					
	0.032918605145602	0				
	-0.573905274855897	0.823256998199009	0			
$a_{ij}^{[E]}$	-0.114172035573537	0.199552791728150	0.381530948900243	0		
	-0.293732375804120	0.443156103274586	0.232514473389434	0.200092213184021	0	
	1.973193167196099	-2.632303480923729	2.113827764673696	-2.326045509877871	1.718581042714500	0
$b_i^{[E]}$	0.971001746640224	-1.272664996516041	1.282112737365169	-1.209258255434315	0.958808767944964	0.27

Fig. A3 Coefficients of the RK46-Ber scheme of Berland et al. [10], corresponding to the explicit part of the SIRK63-S and SIRK63-A schemes.

in Fig. A2 for the SIRK63-A scheme. The coefficients of their explicit part are also given in Fig. A3. They are equal to the coefficients of the RK46-Ber scheme of Berland et al. [10].

References

[1] Bull, M. K., "Wall-Pressure Fluctuations Beneath Turbulent Boundary Layers: Some Reflections on Forty Years of Research," *Journal of Sound and Vibration*, Vol. 190, No. 3, 1996, pp. 299–315. doi:10.1006/jsvi.1996.0066

[2] Tam, C. K. W., and Webb, J. C., "Dispersion-Relation-Preserving Finite Difference Schemes for Computational Acoustics," *Journal of Computational Physics*, Vol. 107, No. 2, 1993, pp. 262–281. doi:10.1006/jcph.1993.1142

[3] Lele, S. K., "Compact Finite Difference Schemes with Spectral-Like Resolution," *Journal of Computational Physics*, Vol. 103, No. 1, 1992, pp. 16–42. doi:10.1016/0021-9991(92)90324-R

[4] Bogey, C., and Bailly, C., "A Family of Low Dispersive and Low Dissipative Explicit Schemes for Flow and Noise Computations," *Journal of Computational Physics*, Vol. 194, No. 1, 2004, pp. 194–214. doi:10.1016/j.jcp.2003.09.003

[5] Runge, C., "Über die Numerische Auflösung von Differentialgleichungen," *Mathematische Annalen*, Vol. 46, No. 2, 1895, pp. 167–178. doi:10.1007/BF01446807

[6] Bashforth, F., and Adams, J. C., *An Attempt to Test the Theories of Capillary Action by Comparing the Theoretical and Measured Forms of Drops of Fluid, with an Explanation of the Method of Integration Employed in Constructing the Tables Which Give the Theoretical Forms of Such Drops*, Cambridge Univ. Press, Cambridge, England, U.K., 1883.

[7] Hu, F. Q., Hussaini, M. Y., and Manthey, J. L., "Low-Dissipation and Low-Dispersion Runge-Kutta Schemes for Computational Acoustics," *Journal of Computational Physics*, Vol. 124, No. 1, March 1996, pp. 177–191. doi:10.1006/jcph.1996.0052

[8] Stanescu, D., and Habashi, W. G., "2N-Storage Low Dissipation and Dispersion Runge-Kutta Schemes for Computational Acoustics," *Journal of Computational Physics*, Vol. 143, No. 2, July 1998, pp. 674–681. doi:10.1006/jcph.1998.5986

[9] Calvo, M., Franco, J. M., and Ràndez, L., "A New Minimum Storage Runge-Kutta Scheme for Computational Acoustics," *Journal of Computational Physics*, Vol. 201, No. 1, Nov. 2004, pp. 1–12. doi:10.1016/j.jcp.2004.05.012

[10] Berland, J., Bogey, C., and Bailly, C., "Low-Dissipation and Low-Dispersion 4th-Order Runge-Kutta Algorithm," *Computers and Fluids*, Vol. 35, No. 10, Dec. 2006, pp. 1459–1463. doi:10.1016/j.compfluid.2005.04.003

[11] Gloerfelt, X., and Berland, J., "Turbulent Boundary-Layer Noise: Direct Radiation at Mach Number 0.5," *Journal of Fluid Mechanics*, Vol. 723, May 2013, pp. 318–351. doi:10.1017/jfm.2013.134

[12] Viazzo, S., Dejoan, A., and Schiestel, R., "Spectral Features of the Wall-Pressure Fluctuations in Turbulent Wall Flows with and Without Perturbations Using LES," *International Journal of Heat and Fluid Flow*, Vol. 22, No. 1, Feb. 2001, pp. 39–52. doi:10.1016/S0142-727X(00)00074-6

[13] Kremer, F., Bogey, C., and Bailly, C., "Influence of Resolution and Reynolds Number on Large-Eddy Simulations of Channel Flow Using Relaxation Filtering," *51st Aerospace Sciences Meeting*, AIAA Paper 2013-0517, Jan. 2013.

[14] Kanevsky, A., Carpenter, M. H., Gottlieb, D., and Hesthaven, J. S., "Application of Implicit-Explicit High Order Runge-Kutta Methods to Discontinuous-Galerkin Schemes," *Journal of Computational Physics*, Vol. 225, No. 2, Aug. 2007, pp. 1753–1781. doi:10.1016/j.jcp.2007.02.021

[15] Wall, C., Pierce, C., and Moin, P., "A Semi-Implicit Method for Resolution of Acoustic Waves in Low Mach Number Flows," *Journal of Computational Physics*, Vol. 181, No. 2, Sept. 2002, pp. 545–563. doi:10.1006/jcph.2002.7141

[16] Dong, H., and Zhong, X., "High-Order Semi-Implicit Simulation of Hypersonic Boundary Layer Stability and Transition," *36th AIAA Aerospace Sciences Meeting and Exhibit*, AIAA Paper 1998-0127, Jan. 1998.

[17] Suh, J., Frankel, S. H., Mongeau, L., and Plesniak, M. W., "Compressible Large Eddy Simulations of Wall-Bounded Turbulent Flows Using a Semi-Implicit Numerical Scheme for Low Mach Number Aeroacoustics," *Journal of Computational Physics*, Vol. 215, No. 2, July 2006, pp. 526–551. doi:10.1016/j.jcp.2005.10.036

[18] Wu, X., and Moin, P., "Direct Numerical Simulation of Turbulence in a Nominally Zero-Pressure-Gradient Flat-Plate Boundary Layer," *Journal of Fluid Mechanics*, Vol. 630, July 2009, pp. 5–41. doi:10.1017/S0022112009006624

[19] Simens, M. P., Jiménez, J., Hoyas, S., and Mizuno, M., "A High-Resolution Code for Turbulent Boundary Layers," *Journal of Computational Physics*, Vol. 228, No. 11, June 2009, pp. 4218–4231. doi:10.1016/j.jcp.2009.02.031

[20] Spalart, P., Moser, R., and Rogers, M., "Spectral Methods for the Navier–Stokes Equations with One Infinite and Two Periodic Directions," *Journal of Computational Physics*, Vol. 96, No. 2, Oct. 1991, pp. 297–324. doi:10.1016/0021-9991(91)90238-G

[21] Asher, U. M., Ruuth, S. J., and Spiteri, R. J., "Implicit-Explicit Runge-Kutta Methods for Time-Dependent Partial Differential Equations," *Applied Numerical Mathematics*, Vol. 25, Nos. 2–3, Nov. 1997, pp. 151–167. doi:10.1016/S0168-9274(97)00056-1

[22] Calvo, M. P., de Frutos, J., and Novo, J., "Linearly Implicit Runge-Kutta Methods for Advection-Reaction-Diffusion Equations," *Applied Numerical Mathematics*, Vol. 37, No. 4, June 2001, pp. 535–549. doi:10.1016/S0168-9274(00)00061-1

[23] Zhong, X., "Additive Semi-Implicit Runge-Kutta Methods for Computing High-Speed Nonequilibrium Reactive Flows," *Journal of Computational Physics*, Vol. 128, No. 1, Oct. 1996, pp. 19–31. doi:10.1006/jcph.1996.0193

[24] Kennedy, C. A., and Carpenter, M. H., "Additive Runge-Kutta Schemes for Convection-Diffusion-Reaction Equations," *Applied Numerical Mathematics*, Vol. 44, No. 1–2 Jan. 2003, pp. 139–181. doi:10.1016/S0168-9274(02)00138-1

[25] Tomkins, C. D., and Adrian, R. J., "Energetic Spanwise Modes in the Logarithmic Layer of a Turbulent Boundary Layer," *Journal of Fluid Mechanics*, Vol. 545, Dec. 2005, pp. 141–162. doi:10.1017/S0022112005006397

[26] Jiménez, J., Hoyas, S., Simens, M., and Mizuno, M., "Turbulent Boundary Layers and Channels at Moderate Reynolds Numbers," *Journal of Fluid Mechanics*, Vol. 657, Aug. 2010, pp. 335–360. doi:10.1017/S0022112010001370

[27] Curle, N., "The Influence of Solid Boundaries upon Aerodynamic Sound," *Proceedings of the Royal Society of London, Series A: Mathematical and Physical Sciences*, Vol. 231, No. 1187, Sept. 1955, pp. 505–514. doi:10.1098/rspa.1955.0191

[28] Powell, A., "Aerodynamic Noise and the Plane Boundary," *Journal of the Acoustical Society of America*, Vol. 32, No. 8, Aug. 1960, pp. 982–990. doi:10.1121/1.1908347

[29] Ffowcs Williams, J. E., and Hawkings, D. L., "Sound Generation by Turbulence and Surfaces in Arbitrary Motion," *Philosophical*

Transactions of the Royal Society of London, Series A: Mathematical and Physical Sciences, Vol. 264, No. 1151, May 1969, pp. 321–342. doi:10.1098/rsta.1969.0031

[30] Hu, Z. H., Morfey, C. L., and Sandham, N. D., "Sound Radiation in Turbulent Channel Flows," *Journal of Fluid Mechanics*, Vol. 475, Jan. 2003, pp. 303–331. doi:10.1017/S002211200200277X

[31] Hu, Z. H., Morfey, C. L., and Sandham, N. D., "Sound Radiation from a Turbulent Boundary Layer," *Physics of Fluids*, Vol. 18, No. 9, Sept. 2006, Paper 098101. doi:10.1063/1.2337733

[32] Van Herpe, F., Oliva Duarte, L., and Lafon, P., "Sound vs. Pseudo-Sound Contributions to the Wind Noise Inside a Car Cabin: A Modal Approach," *18th AIAA/CEAS AeroAcoustics Conference*, Colorado Springs, CO, AIAA Paper 2012-2207, June 2012.

[33] Arguillat, B., Ricot, D., Bailly, C., and Robert, G., "Measured Wavenumber-Frequency Spectrum Associated with Acoustic and Aerodynamic Wall Pressure Fluctuations," *Journal of the Acoustical Society of America*, Vol. 128, No. 4, 2010, pp. 1647–1655. doi:10.1121/1.3478780

[34] Butcher, C. *Numerical Methods for Ordinary Differential Equations*, 2nd ed., Wiley, West Sussex, England, U.K., 2008.

[35] Alexander, R., "Diagonally Implicit Runge-Kutta Methods for Stiff O.D.E.s," *SIAM Journal on Numerical Analysis*, Vol. 14, No. 6, 1977, pp. 1006–1021. doi:10.1137/0714068

[36] Bogey, C., and Bailly, C., "Three-Dimensional Non-Reflective Boundary Conditions for Acoustic Simulations: Far Field Formulation and Validation Test Cases," *Acta Acustica*, Vol. 88, No. 4, 2002, pp. 463–471.

[37] Berland, J., Bogey, C., Marsden, O., and Bailly, C., "High-Order, Low Dispersive and Low Dissipative Explicit Schemes for Multiple-Scale and Boundary Problems," *Journal of Computational Physics*, Vol. 224, No. 2, 2007, pp. 637–662. doi:10.1016/j.jcp.2006.10.017

[38] Bogey, C., Marsden, O., and Bailly, C., "Large-Eddy Simulation of the Flow and Acoustic Fields of a Reynolds Number 10^5 Subsonic Jet with Tripped Exit Boundary Layers," *Physics of Fluids*, Vol. 23, No. 3, 2011, Paper 035104. doi:10.1063/1.3555634

[39] Bogey, C., de Cacqueray, N., and Bailly, C., "A Shock-Capturing Methodology Based on Adaptative Spatial Filtering for High-Order Non-Linear Computations," *Journal of Computational Physics*, Vol. 228, No. 5, 2009, pp. 1447–1465. doi:10.1016/j.jcp.2008.10.042

[40] Bogey, C., and Bailly, C., "Large Eddy Simulations of Transitional Round Jets: Influence of the Reynolds Number on Flow Development and Energy Dissipation," *Physics of Fluids*, Vol. 18, No. 6, 2006, Paper 065101. doi:10.1063/1.2204060

[41] Bogey, C., and Bailly, C., "Turbulence and Energy Budget in a Self-Preserving Round Jet: Direct Evaluation Using Large Eddy Simulation," *Journal of Fluid Mechanics*, Vol. 627, May 2009, pp. 129–160. doi:10.1017/S0022112009005801

[42] Moser, R. D., Kim, J., and Mansour, N., "Direct Numerical Simulation of Turbulent Channel Flow up to $Re_\tau = 590$," *Physics of Fluids*, Vol. 11, No. 4, 1999, pp. 943–945. doi:10.1063/1.869966

[43] Robinson, S. K. "Coherent Motions in the Turbulent Boundary Layer," *Annual Review of Fluid Mechanics*, Vol. 23, Jan. 1991, pp. 601–639. doi:10.1146/annurev.fl.23.010191.003125

[44] Kline, S. J., Reynolds, W. C., Schraub, F. A., and Runstadler, P. W., "The Structure of Turbulent Boundary Layers," *Journal of Fluid Mechanics*, Vol. 30, No. 4, Dec. 1967, pp. 741–773. doi:10.1017/S0022112067001740

[45] Bogey, C., Marsden, O., and Bailly, C., "On the Spectra of Nozzle-Exit Velocity Disturbances in Initially Nominally Turbulent, Transitional Jets," *Physics of Fluids*, Vol. 23, No. 9, 2011, Paper 091702. doi:10.1063/1.3642642

[46] Goody, M. C., and Simpson, R. L., "Surface Pressure Fluctuations Beneath Two- and Three-Dimensional Turbulent Boundary Layers," *AIAA Journal*, Vol. 38, No. 10, 2000, pp. 1822–1831. doi:10.2514/2.863

[47] Hu, Z. H., Morfey, C. L., and Sandham, N. D., "Wall Pressure and Shear Stress Spectra from Direct Simulations of Channel Flow," *AIAA Journal*, Vol. 44, No. 7, 2006, pp. 1541–1549. doi:10.2514/1.17638

[48] Willmarth, W. W., and Wooldridge, C. E., "Measurements of the Fluctuating Pressure at the Wall Beneath a Thick Turbulent Boundary Layer," *Journal of Fluid Mechanics*, Vol. 14, 1962, pp. 187–210. doi:10.1017/S0022112062001160

[49] Hu, Z. H., Morfey, C. L., and Sandham, N. D., "Aeroacoustics of Wall-Bounded Turbulent Flows," *AIAA Journal*, Vol. 40, No. 3, 2002, pp. 465–473. doi:10.2514/2.1697

[50] Choi, H., and Moin, P., "On the Space-Time Characteristics of Wall-Pressure Fluctuations," *Physics of Fluids A*, Vol. 2, No. 8, 1990, pp. 1450–1460. doi:10.1063/1.857593

Z. J. Wang
Associate Editor